**FULL RESEARCH ARTICLE**

# Melting ceramic Al$_2$O$_3$ powder by electron beam powder bed fusion

**William Sjöström[1]** · **Carlos Botero[1,2]** · **Emilio Jimenez-Piqueo[3,4]**

**Abstract**

Electron beam powder bed fusion (PBF-EB) is a known metal additive manufacturing (AM) technology. Processing non-conducting powders such as ceramics has so far been considered as not feasible because of the inherent problems with Coulomb repulsion due to insufficient electrical conductivity. In this study, a method for functionalizing ceramic powder is proposed where particles are electroless coated by a ~ 1 µm Ni layer to decrease the surface resistivity. The feasibility of the suggested approach is tested on Al$_2$O$_3$ powder, and the results show that the coated ceramic powder has a decreased surface resistivity, which enables processing by PBF-EB. Heating and melting parameters were investigated and samples were manufactured at ~ 1600 °C. Sintered and melted powders were analyzed by microscopy and micromechanically tested by nanoindentation. Calculations, visual observation and SEM–EDX suggest that the Ni coating is evaporated during the process, which suggests that the process could be feasible for the manufacturing of pure ceramic parts.

**Keywords** Electron beam powder bed fusion · Ceramic · Coating · Process manipulation · Additive manufacturing

## 1 Introduction

Additive manufacturing (AM) by powder bed fusion (PBF) works on the principle of spreading and melting fine powder, layer by layer until the desired component geometry is finished. Processing ceramics by PBF is becoming a hot topic [1–6] as it would allow direct manufacturing of complex components without the need for post-sintering of AM-produced green bodies. When the melting in PBF is performed by the kinetic energy of an incident electron beam (EB) the process is denoted PBF-EB. Utilizing an EB has several benefits compared to alternative methods (eg. Laser) such as higher energy input, faster beam speed and a clean process environment [7–14]. Due to the high melting temperature and low fracture toughness of ceramics, the energy input and a clean environment, free of contamination, are crucial factors during processing. The vacuum atmosphere inside the PBF-EB chamber is an effective way to thermally insulate all metal parts of the system and thereby allow high process temperatures. There are however some issues that arise from bombarding powder by electrons. The main drawback in the case of processing ceramics is that the EB will leave negative charges (arising from the incident electrons) in its path. If the conductivity of the powder bed (PB) is not sufficient to dispose of the electrons quickly enough, smoke will occur [15–17]. Smoke is the phenomenon where the powder particles gain a negative charge that is large enough to cause the PB to "blow away" by the Coulomb repulsion between the individual particles. This can be avoided in a number of ways [15, 18–23], most commonly the PB will be slightly sintered by defocusing the EB during the pre-heating (PH) step of the PBF-EB process. Once the powder particles are mechanically connected by small necks/bridges, it is possible to melt the powder by applying higher power and smaller spot sizes [24–27].

✉ William Sjöström
william.sjostrom@miun.se

Carlos Botero
carlos.botero@miun.se

Emilio Jimenez-Piqueo
emilio.jimenez@upc.edu

[1] SportsTech Research Center, Mid Sweden University, Östersund, Sweden

[2] Matkom AB, Frösön, Sweden

[3] Barcelona Research Center in Multiscale Science and Engineering, Universitat Politècnica de Catalunya, Campus Diagonal Besòs − EEBE, 08019 Barcelona, Spain

[4] Department of Materials Science and Engineering, EEBE, Universitat Politècnica de Catalunya, UPC, C/Eduard Maristany, 10-14, 08019 Barcelona, Spain

Depending on the powder bed conductivity and particle weight, the sintering needs to be more or less extensive for suppressing smoke. As the powder should be removed from the solid components after the process, a loose sintering is beneficial for process effectiveness and powder recyclability.

Normally the acceleration voltage, which determines the kinetic energy of each incident electron, is fixed in PBF-EB. Thereby, the beam power is mainly determined by the beam current (BC). The beam energy is controlled by a combination of BC and beam speed (BS). However, the local energy input and activated volume are also dependent on the focus offset (FO) as a smaller spot size yields a higher electron density. Further, the choice of beam strategy such as jumping between spots or sweeping lines in different orders can highly influence thermal history and powder consolidation. In fully developed PBF-EB melting themes, BC, BS and FO are combined with hundreds of other settings such as line offset, line order, turn-point compensation, etc. In the initial stages of material development, it is sufficient and common practice to define a "process window", in which a span of BC and BS yields dense material. This process window is only valid at one process temperature and with the other settings set at fixed values. PBF-EB process temperatures are generally in the range of 40–80% of the melting temperature [28, 29], and materials susceptible to cracking often lie in the upper end of that range.

There is only one previous work on ceramics related to EB, focusing on $ZrSi_2$ liquid phase sintering of $ZrB_2$ [30]. To the best knowledge of the authors, there are no reports available in the open literature on melting ceramics by PBF-EB. Therefore, this feasibility study is the first published work on PBF-EB/C (denotation according to ASTM/ISO 52900) and the initial findings can be of importance for future developments. A few studies have been published on Laser-based PBF methods (PBF-LB) on ceramics focusing on composites[3, 4], porous structures [11, 31], and even some solid ceramics [1, 2]. The reason for the lack of publications related to ceramics in PBF-EB is possibly due to the high smoke sensitivity of low-conducting powders, which leads to the assumption that the process should not be feasible. This work proposes overcoming this issue by applying a thin metal coating that increases the surface conductivity of the powder, thereby lowering the smoke sensitivity. The applied coating should be so thin that it either fully evaporates during the process or does not change the chemical composition and mechanical properties by much. This work tests the proposed feasibility on $Al_2O_3$ which should be one of the most challenging ceramics to process due to the low conductivity and small window between melting temperature and boiling temperature. For future PBF-EB/C developments, it should be noted that there are ceramic materials such as $ZrO_2$, which are known to be electric current-assisted sinterable and thereby should be suitable for PBF-EB/C processes.
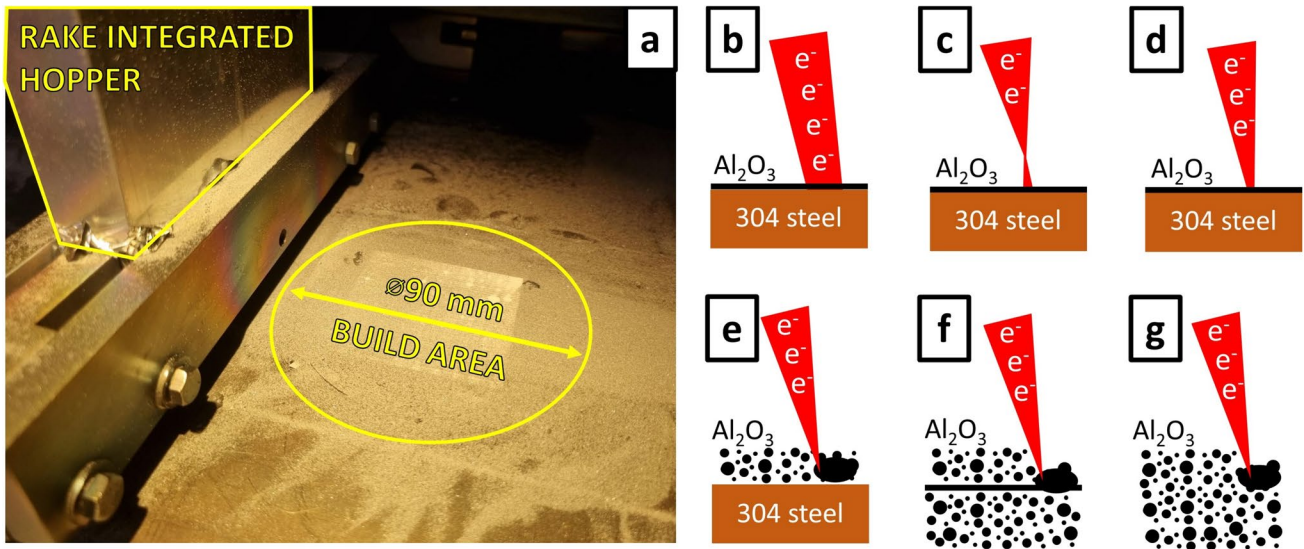
# 2 Method

All experiments were performed in a modified Arcam S12 (ARCAM EBM, a part of GE, Mölnlycke, Sweden) PBF-EB system upgraded to A2 specifications. A custom chamber interior with a small build envelope (⌀90 mm build area) was used to reduce the powder needed for process development. The powder was gravity-fed by a rake-integrated hopper seen in Fig. 1a. All inputs to the machine were given through EBM control 3.2 as it allows almost full access to machine settings. The processing environment was a He-controlled vacuum at $2*10^{-6}$ bar. Pre-study trials on ceramic powders revealed that the tendency for smoke is very high [4–6]. Initial $Al_2O_3$ process settings were developed on pre-sintered $Al_2O_3$ plates as described in Sect. 2.1 and illustrated in Fig. 1b–d. After the feasibility was tested and initial process settings were developed, experiments were performed on powder as described in Sect. 2.2 and illustrated in Fig. 1e–g.

## 2.1 Process development by melting pre-sintered plates

The initial process development described in this section was performed by surface remelting to find reasonable parameters for stable melting and sufficient melt pool penetration. EB heating and line melting was performed on 1 mm thick 50 mm × 50 mm thermally pre-sintered 96% pure $Al_2O_3$, as illustrated in Fig. 1b–d. Thinner plates of 100 μm and 200 μm thickness were also tested but found to be too susceptible to crack formation and therefore excluded. The mass and integrity of the pre-sintered plates enabled disregarding of the inherent problems when working with powders. Thereby, attention could be put on the processability and development of an approximate PBF-EB/C/$Al_2O_3$ process window.

When bombarding the $Al_2O_3$ plates with electrons, the charge build-up could in some cases become sufficient to cause vibrations and levitation of the plate, similar to a smoke event, but with slower displacement due to the larger mass of the plate. In these cases, the $Al_2O_3$ plate floated away from the build area because of the Columb repulsion towards the grounded underlaying 304 stainless steel plate. The heating theme was therefore developed by lowering the BC and increasing the BS until no plate movement could be observed. High FOs were used to yield a very large spot size which decreases the charge density as illustrated in Fig. 1b. Incremental steps of BC and BS were tested until a

**Fig. 1** Build area and rake integrated hopper used for the experiments (**a**). Illustration of: method for developing a heating process with a defocused beam (**b**), method for developing a melting process with negative focus offset (**c**), and positive focus offset (**d**). Illustrations of the three build platforms used in this work: melting powder on a heated 304 stainless steel plate (**e**), melting powder on a heated $Al_2O_3$ plate and melting powder on a heated powder bed

combination that allowed heating of the plate without movement was found.

The S12 system is conventionally equipped only with a K-type thermocouple, which is limited to measuring temperatures below ~ 1260 °C. Thereby the temperature could not be measured continuously during the experiments. However, visual observation of the heated $Al_2O_3$ allowed some approximation as the emittance changes with temperature as shown in Fig. 2a and b. Four wavelengths were targeted for

pyrometer observations as the area A, B, C and D indicates in Fig. 2a. A Micro-Epsilon CTLM-2H1CF4-C3 (Micro-Epsilon Messtechnik GmbH & Co. KG, Ortenburg, Germany) short wave infrared (SWIR) pyrometer, capable of measuring 490–2000 °C was installed outside of the vacuum chamber, as shown in Fig. 2c and d. The SWIR pyrometer is equipped with two LASER-pointers, which coincide with the focal point, these were used to focus the pyrometer on the center of the build area. Around 80% of the SWIR signal

**Fig. 2** The emitted color spectrum during heating of $Al_2O_3$, with pyrometer-measured temperatures indicated at the wavelengths A, B, C and D (**a**). The value within parentheses corresponds to the standard deviation. Pictures during heating of a pre-sintered $Al_2O_3$ plate to exemplify how the temperature can be controlled from observing the emitted photons (**b**). Pictures of how the pyrometer was installed outside of the vacuum chamber (**c**, **d**)
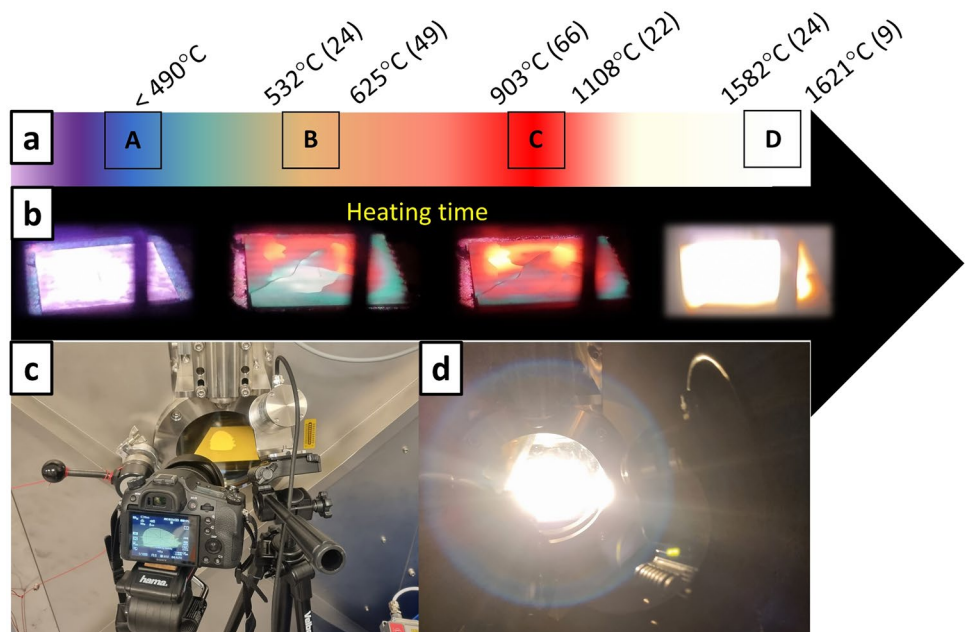
can pass through the observation window and thereby be detected by the pyrometer [32]. An $Al_2O_3$ plate was heated to visually represent the wavelengths A, B, C and D in Fig. 2a, and pyrometer data was saved for each of these regions. The resulting data is very peaky due to the increase in temperature each time the EB passes the point of measurement. Therefore, the highest and lowest observed peaks were noted for three measurements of each wavelength region, to calculate the temperature intervals as shown in Fig. 2a. In all experiments, the plate was considered to be at processing temperature when visually determined to be within area D, meaning between 1582 °C (24) and 1621 °C (9). This visual approximation of the temperature allowed repeatable conditions when developing the process. It can be noted that the D-region corresponds to 76–78% of the melting point of $Al_2O_3$ and is thereby within the common span for processing temperatures in PBF-EB [28, 29].

Single melt lines of 10 mm length were performed on the pre-sintered plates with varying conditions and melt parameters. The melt lines were performed both at room temperature and at the processing temperature (D-region in Fig. 2a). Initial experiments showed that melting $Al_2O_3$ requires high energy as compared to the "standard" metal powders. Therefore, the beam current was locked at 20 mA, which is the maximum to deliver a predictable focused beam behavior in the S12 system. The BS was varied between 250 and 2000 mm/s yielding line energies of 0.6–4.8 J/mm. To minimize ramping effects, each set of experiments was preceded by a total of 20 mm "dummy sweeping" (BC 20 mA, BS 1000 mm/s and FO + 50 mA) outside of the area to be analyzed. This allowed the BC to stabilize at 20 mA before melting the 10 mm lines. FO and BS stabilize much quicker so there is no need to "dummy sweep" in between each line melt.

FO has varied between − 20 and 20 mA. The corresponding spot size for the S12 system according to the method described by Lin et al. [25, 33] is shown in Fig. 3. Although this method only gives values such as peak track width (PTW) and scanning track width (STW), it still gives an easy approximation of the length scale of the actual spot size. It is increasingly important to relate FO to the spot size as more and more variants of PBF-EB systems are in use, and there is yet no standard way to transfer parameters in-between the systems. The actual spot size in PBF-EB is difficult to investigate in most systems due to the lack of eg. backscatter detectors, which can investigate how the signal changes when the beam, with known speed, is swept over a feature, such as a hole with known dimensions. Other methods to evaluate the spot size could be eg. by puncturing thin plates [34]. Spot size values available in PBF-EB literature commonly range between 200 and 1000 µm [25, 33, 35–38].

The line melting experiments were repeated for two different beam strategies: continuous melting and spot melting.
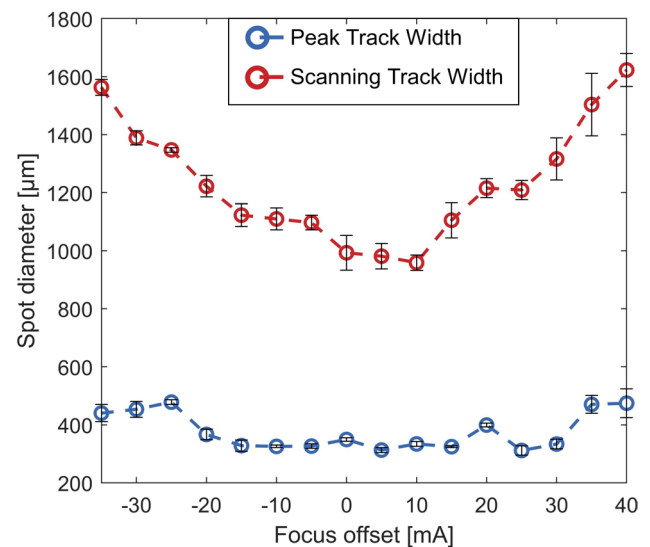


**Fig. 3** Spot size investigations in the Arcam S12 PBF-EB system were used in this study. The spot size was investigated by measuring the peak track width and scanning track width according to the method and melt settings described in [25, 33]. The error bars correspond to the standard deviation for five individual measurements

The spot melting was done by structured sweeping of five consequal spots, spaced by 2 mm, along the 10 mm line and overlapping each region by 0.3 mm. This is similar to the Arcam-multi-beam method for melting contours but in this case only performed in one line. The reason for including spot melting was to evaluate if there is an observable difference in cracking behavior as compared to continuous melting over the whole line. Spot melting can generally keep multiple smaller melt pools open as opposed to the single larger melt pool created by continuously sweeping the beam. The continuous melting experiments were also performed in a heated state (temperature according to the D-region of Fig. 2a).

Cross-sections of the samples were prepared by using a glass cutter to induce cracking perpendicular to the melt lines (aiming for the crack to be in the center of each line). The samples were encapsulated in epoxy resin, and grinded with SiC paper in steps 320–4000 grit during rigorous water cooling. The as-built top surface of the melt lines as well as cross-sections were measured and inspected by scanning electron microscopy (SEM) (Tescan Maia 3, Brno, Czech Republic).

## 2.2 Process development on ceramic powder

Once an approximate process window was obtained as described in Sect. 2.1, experiments were conducted on $Al_2O_3$ powders. The composition of the powders used was > 99.8% $Al_2O_3$ with traces of $Na_2O$, $Fe_2O_3$ and $SiO_2$ (delivered by Final Advanced Materials, Didenheim, France). Powder
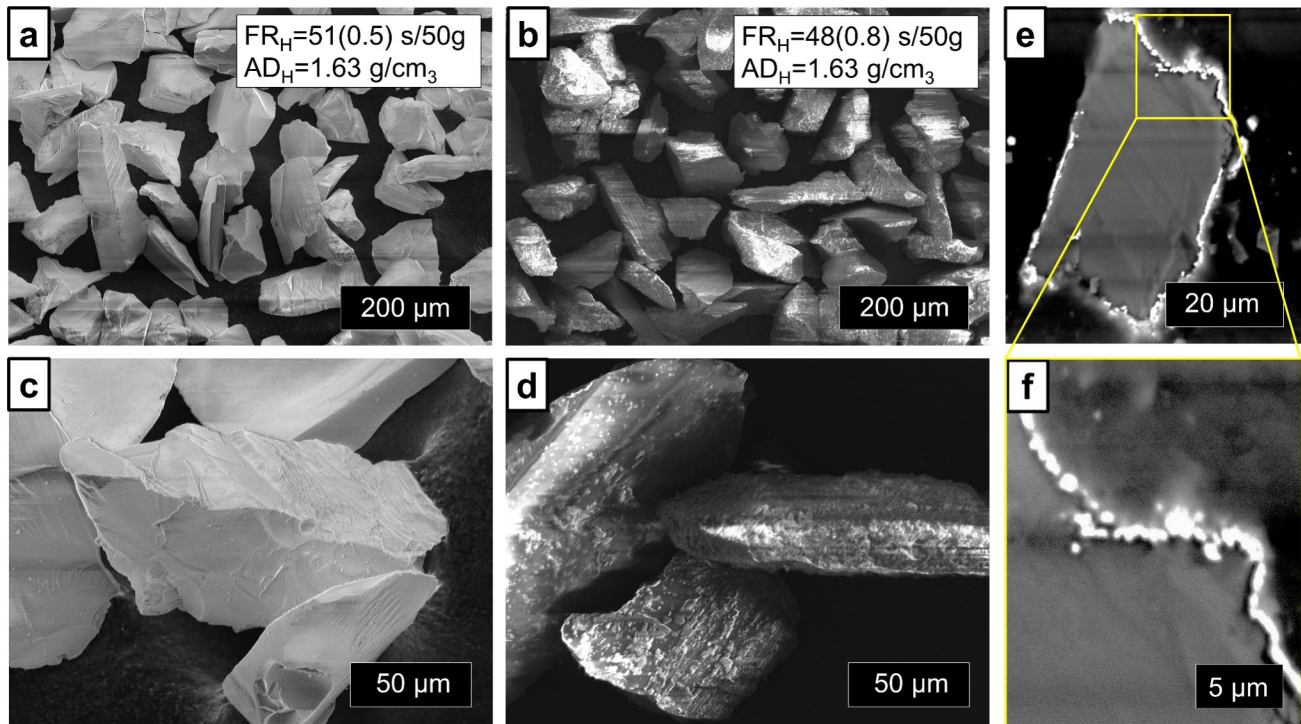
**Fig. 4** As delivered (**a**) and electroless coated, **b** Al$_2$O$_3$ angular powder used in this study. **c** and **d** Respectively, shows the uncoated and coated powder in higher detail. **e** and **f** Shows the coated powder in cross-section

consisted of angular particles (Fig. 4a) and distribution was d10 < 60 μm, $d_{50}$ = 95 μm and $d_{100}$ < 150 μm. The fraction was selected to be in the upper span of what is commonly used in the PBF-EB (~ 45–150 μm) to maximize the mass of the particles and thereby minimize the smoke tendency. Another benefit of using a large fraction without any small particles present is that the cleaning is significantly simplified when the number of particles is decreased, especially since the developments presented here resulted in many smoke events. In an optimized process that is performed in a system dedicated to ceramic processing, it may be beneficial to use a smaller fraction to increase the sintering activity and packing density. However, the spot size in the S12 system is quite large as explained in Sect. 2.1, which increases the need for high BC when melting, and thereby it is hypothesized that it is beneficial to use a large fraction.

To reduce the smoke sensitivity, a thin conductive coating was applied to the powder surface. Coating of the powder was performed by electroless plating. In doing so, the powder (500 g per batch) was immersed in a glass container with a Ni-rich acid bath (1.5 L) at a constant temperature of 80 °C with magnetic stirring. The powder specimens were coated for 20 min, removed from the bath, washed with water and acetone, air-dried and left in a vacuum oven to dry for 24 h at 70 °C. The final coating method used in this work (Fig. 4b) resulted in a ~ 6% improvement of the ASTM B213 Hall

flow rate (FR$_H$) with unchanged ASTM B212 apparent density (AD$_H$) as delivered powder in Fig. 4a. The uncoated and coated powder is shown in more detail in Fig. 4c and d respectively. The cross-section of the coated powder as shown in Fig. 4e reveals that the coating does not have full coverage but can be found in the majority of the powder's contour. Figure 4f indicates that the coating is ~ 1 μm thick.

To investigate how the powder conductivity changes with coating, a method was developed where the electrical resistance over a standard volume of powder was measured at various compression forces. The standard sample volume was measured by letting the powder flow through a Hall funnel into a measuring cup according to Fig. 5a. Once the measuring cup was full, the Hall funnel was swiveled away, and the overflow was carefully removed using a vertical flat edge (the measuring method is the same as in ASTM B212 but with a smaller measuring cup). The standard powder volume was then transferred to the slightly taller measuring cylinder shown in Fig. 5b and the punch was lowered into this cylinder. Below a compression force of 10 N, no tested powders showed any electrical connection. Therefore, the resistivity of the powder batches was analyzed at 10, 20, 30, 40, 50, 60, 70, 80, 90 and 100 N. The compression was performed in an Instron 5969 multitester (Instron, Norwood, Massachusetts, United States). To put the results into context,
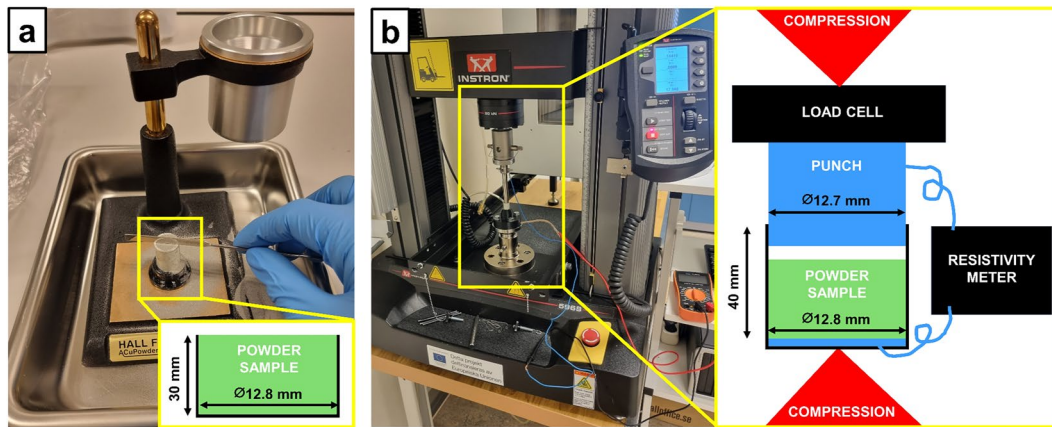
**Fig. 5** Picture showing how the standard powder sample size for resistivity measurement was gathered, including an illustration with the measuring cup dimensions (**a**). Picture showing the setup for measuring powder resistivity, including a clarifying illustration with measurements (**b**). The scale of the illustrations is not proportional for visual reasons

the conductivity of Ti-6Al-4V and elemental Ni powder was also analyzed. The Ti-6Al-4V of 45–150 μm fraction was delivered by Arcam (Arcam AB, Mölndal, Sweden, now a part of GE-additive, USA). The elemental 99.99% Ni powder of 0–150 μm fraction was delivered by Sigma-Aldrich (Sigma-Aldrich, Burlington, Massachusetts, United States). It should be noted that the resistance of the described setup excluding any sample is ~ 1.8 Ω, which is not significant for most of the performed measurements. The resistivity was measured by a standard multimeter capable of measuring 0.1–20 MΩ with an accuracy of ± 0.8%.

When melting the powder with the parameters developed according to Sect. 2.1, three different variants of build platforms were tested; 10 mm thick 304 stainless steel plate according to Fig. 1e (as commonly used in PBF-EB/M processes), pre-sintered $Al_2O_3$ (Fig. 1f) and a heated powder bed of the $Al_2O_3$ coated precursor powder (Fig. 1g). After producing samples, cross-sections were prepared by hot encapsulation, water-cooled grindning with SiC paper 320–4000 grit and polishing with diamond paste 3–1 μm. Selected cross-sections were nanoindented (MTS XP nanoindenter, Tennessee, USA) using depth control to 2000 nm penetration in grids of different sizes where all indents were separated by 25 μm. Particles and cross-sections were also studied by SEM (Tescan Maia 3 and Tescan Vega, Brno, Czech Republic) and energy dispersive X-ray (EDX, Oxford Instruments, Oxfordshire, England).

As the aim was to evaporate the Ni-coating during the PBF-EB process, some estimation was needed. To calculate the boiling point, $T_2$, for Ni in the processing atmosphere, the Clausius–Clapeyron equation can be written in the following form:

$$T_2 = -\left( \frac{R * \ln\left(\frac{P_2}{P_1}\right)}{\Delta H_{vap}} + \frac{1}{T_1} \right)^{-1}, \tag{1}$$

where $R$ is the ideal gas constant, $P_2$ is the processing pressure (~ $1.5*10^{-3}$ torr), $DH_{vap}$ is the heat for vaporization ($370.4*10^3$ J/mol). $P_1$ and $T_1$ is another pressure and temperature, at which Ni is known to boil. Values for $P_1$ and $T_1$ can be extracted from tables to 760 torr and 3003 K, respetively. When inputting these values in Eq. (1), a $T_2$ value of 1.593 K or 1320 °C can be calculated. This indicates that for processes above this temperature, severe evaporation of Ni can be expected.

## 3 Results and discussion

### 3.1 Process development by melting pre-sintered plates

Heating $Al_2O_3$ plates by the EB (as illustrated in Fig. 1b) was possible under some conditions. At high energies, the plates crack into several parts, charges up and starts to vibrate/levitate as described in Sect. 2.1. At low energies, heating is possible but slow. The best compromise was found by incrementally increasing the intensity of FO for each BC step as shown in Table 1. The steps with approximate heating time were stopped when the color of the region as indicated was visually confirmed (as described in Fig. 2). The last heating step is in place to increase the temperature buffer as the pyrometer never gave a reading above 1631 °C, even with prolonged heating for over 10 min.

**Table 1** Parameters and incremental steps used for the final heating theme

| Start | Stop | Time [min] | FO [mA] | BS [mm/s] | BC [mA] |
|-------|------|-----------|---------|-----------|---------|
| RT | <490 °C | 1 | 250 | 8000 | 5 |
| <490 °C | Region A (<490 °C) | ~2 | 100 | 8000 | 5 |
| Region A | Region A (<490 °C) | 1 | 250 | 8000 | 7.5 |
| Region A | Region B (~550 °C) | ~3.5 | 100 | 8000 | 7.5 |
| Region B | Region B (~550 °C) | 1 | 250 | 8000 | 10 |
| Region C | Region D (~1600 °C) | ~6 | 100 | 8000 | 10 |
| Region D | Region D | 6 | 100 | 8000 | 10 |

Regions A–D indicate the emittance as described in Sect. 2.1

**Fig. 6** SEM micrographs on the top surfaces of the melt tracks with varying focus offset (**a**) and beam speed (**b**) as well as cross sections of a selected cold-melted track (**c**) and a hot-melted track (**d**). Spot, Cont. and Heated cont. means respectively spot melting, continuous melting and heated (~1600 °C) continuous melting according to description in Sect. 2.1
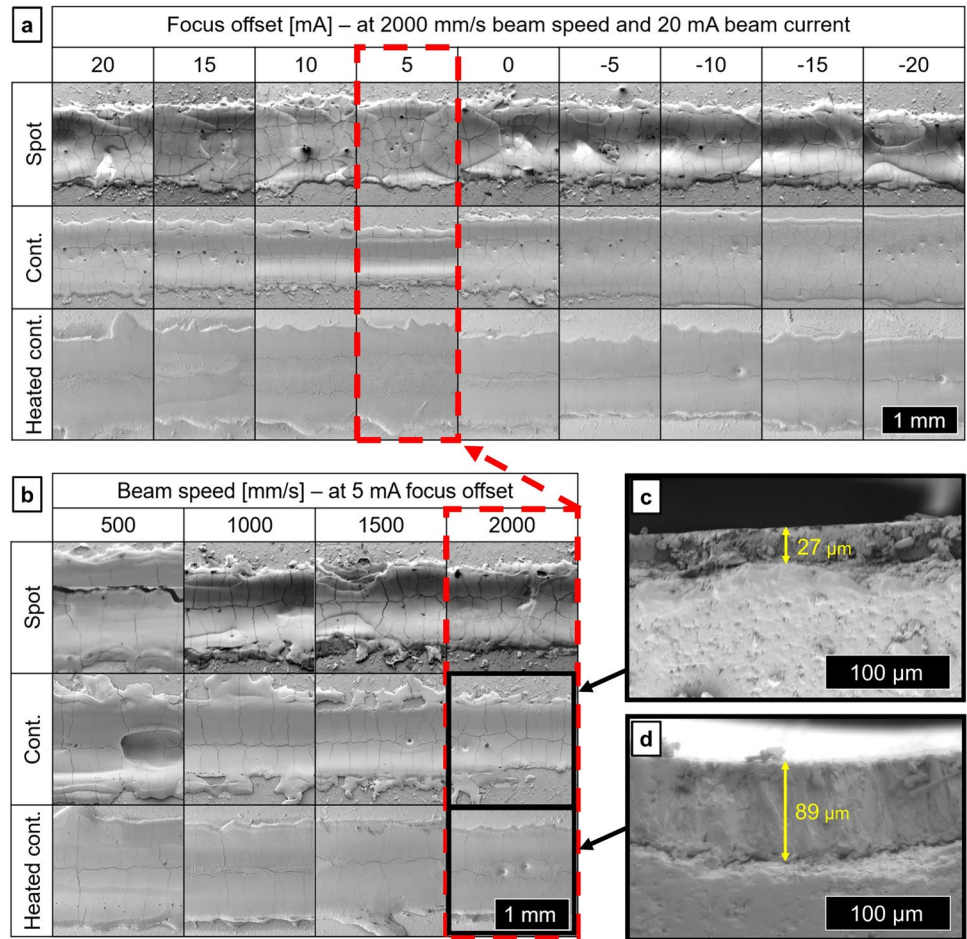


The single line melting (as illustrated in Fig. 1c, d) gave good ground for approximating a process window. FO of 5–20 mA resulted in spatter around the melt tracks as visible in Fig. 6a. Interestingly, corresponding negative FOs (− 10 to − 20 mA) did not result in a spatter. This is believed to be due to the divergent beam creating a lower electron density inside the sample when compared to a converging beam (positive FO). A similar observation was done by Lin et al., where a negative FO is argued to lead to a larger scattering of electrons inside the material [25]. When studying cross-sections (Fig. 6c, d) it was found that the melt pool depth is shallow (~ 15–90 μm), compared to the standard layer thicknesses used in PBF-EB/M (~ 50–100 μm). Therefore, it could be concluded that a low BS is beneficial as this increases the energy input, allowing a greater penetration depth. However, as can be seen in Fig. 6b, BS below 2000 mm/s resulted in somewhat unstable beams with increased spatter, hole formations and irregular tracks. Further, tracks melted with lower BSs were susceptible to crack (all samples melted with 250 mm/s instantly cracked while 500 mm/s was fine for all melting strategies except for spot-melting). All spot-melted samples at 500 mm/s cracked, leading to the conclusion that

spot-melting increases the risk for cracks to appear. This is further proven by the uneven surfaces from the resulting tracks as well as several spot-melted samples that cracked at 1000 mm/s. At elevated temperatures, the melt pool penetration depth and width are increased and there are less microcracks in the resulting melt lines (Fig. 6a, b). Melting on heated plates also increased the melt pool penetration depth as can be seen by comparing Fig. 6c and d.

According to the results as shown in Fig. 6a, a diverging beam leads to a smoother melt track (and potentially a lower risk for smoke), thereby it could be concluded that negative FOs are promising in PBF-EB/C/$Al_2O_3$ processes. However, due to the selected powder fraction in this work, melt pool penetration was determined to be the most critical factor, and the lines with negative FO showed around 40% less penetration as compared to the ones with positive FO. Another reason for using a positive FO is that during the experiments, the S12 system was calibrated according to the method stated by Arcam. This method involves calibrating the astigmatism in the positive FO region, and the authors have experienced this to result in a non-circular spot in the negative FO region. This could also explain why the

penetration depth is smaller at negative FO and suggests that a calibration in the negative FO region might help overcoming the issue in future work. Thereby, the parameters 20 mA BC, 1000 mm/s BS at 5 mA FO, melted with a continuous strategy, was concluded to be the best combination of parameters. These parameters resulted in the thinnest (and deepest due to the focused beam) melt track with an acceptable amount of spatter and was selected as the preliminary melting theme. It can be noted that the results presented in Fig. 6 are consistent with the spot size presented in Fig. 3, where the smallest melt line can be expected to be at 5–10 mA FO.

Single layer re-melting of 10 mm × 10 mm squares on heated $Al_2O_3$ plates with a continuous converging melt line strategy, using 0.25 mm line offset according to Fig. 7a resulted in the top surface shown in Fig. 7b. The penetration of such a melt pool is around 200 μm as shown in Fig. 7c. The scanning strategy shown in Fig. 7a was developed since the standard bi-directional and uni-directional patterns induced cracks in all tested cases. The continuous converging scanning strategy has the benefit of distributing the heat towards the center of the melted cube, mitigating the thermal gradients over the cube area, and increasing the local cooling
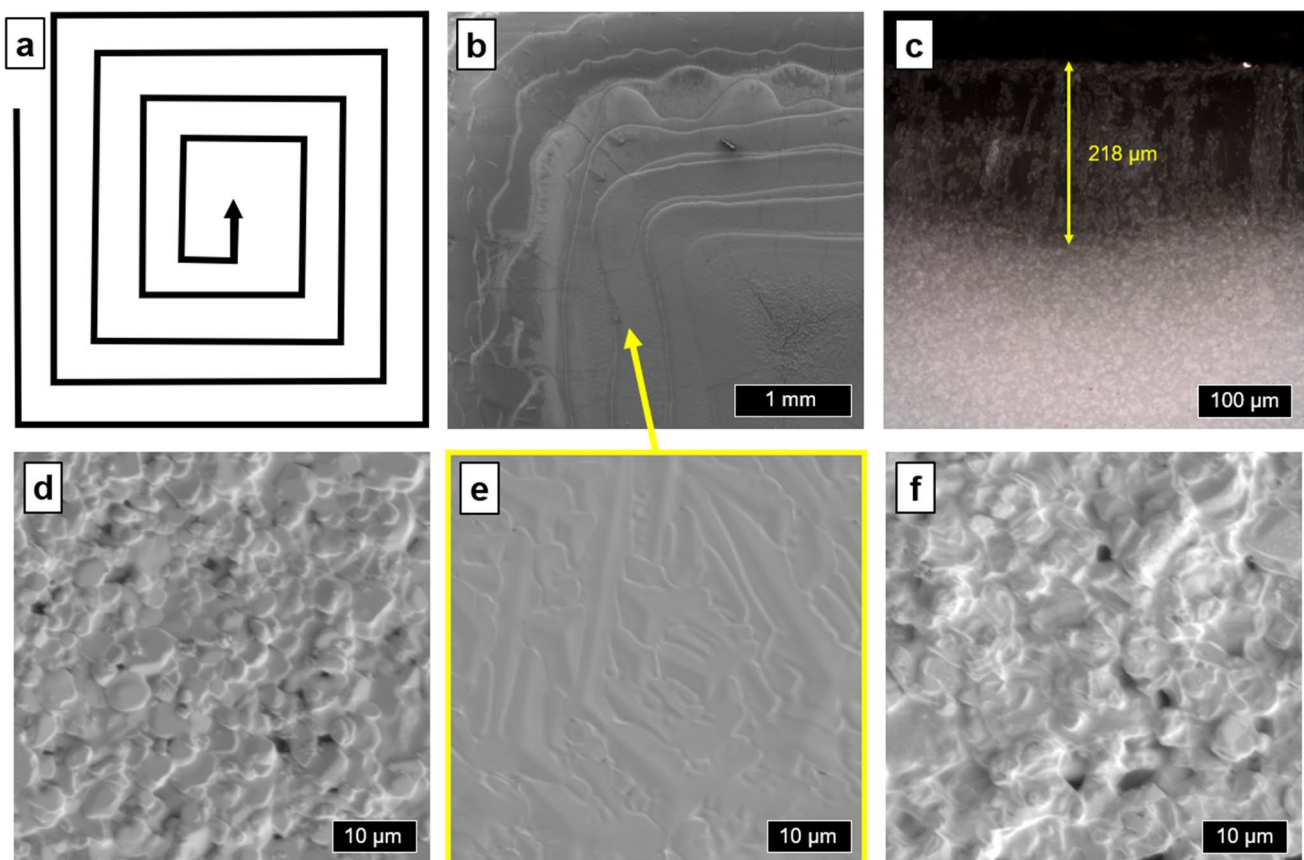


**Fig. 7** Somewhere here. Figure 7. Schematic illustration of the beam path in the selected scanning strategy for square samples (**a**), the resulting top surface (**b**), cross-section (**c**) and top surface microstruc-tures; as delivered $Al_2O_3$ plate (**d**), melted plate (**e**) and heated but not melted plate (**f**)

time. Thereby this strategy is shown to be a feasible method for melting ceramic cubes in PBF-EB. Complex structures may need other strategies but that is outside of the scope for this work. The as-built microstructure of the sample can be seen in Fig. 7e where it is compared to that of delivered pre-sintered $Al_2O_3$ plates (Fig. 7d) and heated $Al_2O_3$ plate (Fig. 7f). The heated plate shows larger grains after the crystalline growth that occurs upon heating, but the pores (characteristic for sintered materials) are still present. The lack of pores together with the dense polycrystalline structure in the melted areas (Fig. 7e) confirms that the PBF-EB/C process is capable of melting $Al_2O_3$ and yielding a fully dense ceramic.

## 3.2 Process development on ceramic powder

The powder resistivity results are presented in Fig. 8, where it can be seen that coated powder is not conductive (or has a higher resistance than the detection limit of 20 MΩ) at loads below 50–60N. However, at loads at 70N and above, the coated powder is more conductive than Ti-6Al-4V. These results are indicating that in loose-packing scenarios, the contact points between the powder particle surfaces are too small, or that too many of the contact points are not coated. As the packing increases, the contact surfaces increase, and the powder bed becomes conductive. This proves that the coating is conductive and thereby should be able to lower the smoke sensitivity. In the case of PBF-EB, the powder bed is loosely packed, and thereby conductivity at low loads should be beneficial. However, as can be seen in Fig. 8, Ti-6Al-4V, which is the most commonly used material in PBF-EB, does not show as conductive until loaded by 30N. The vacuum
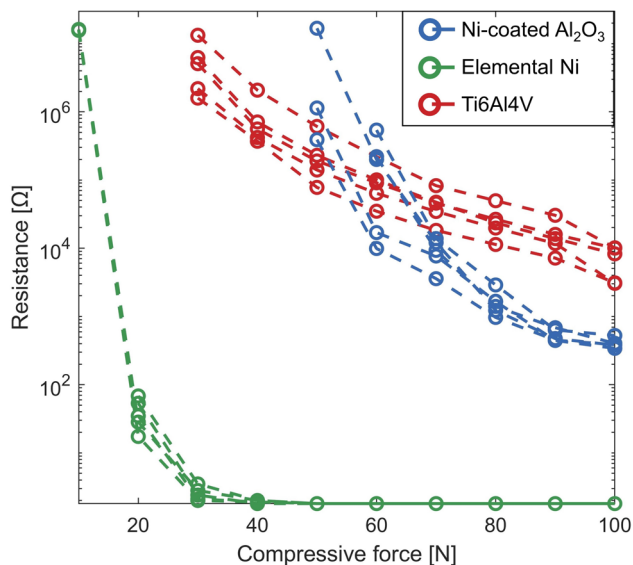


**Fig. 8** Graph showing the resistivity over powders measured as described in Sect. 2.2. Data from five measurements of each powder type is shown

environment or electron movement in the powder bed may change the behavior of the powder, breakdown voltage and related properties. The uncoated powder had a resistivity above the detection limit (20 MΩ) and is therefore not included in Fig. 8. These results indicate that Ni-coating the $Al_2O_3$ powder should increase the processability, however, as shown in Fig. 4f, it should be remembered that the coating is very thin and could be removed by the application of EB. To further investigate the powders, they were tested in the PBF-EB process.

### 3.2.1 Melting $Al_2O_3$ powder on top of a heated 304 stainless plate

Melting ceramic powder on top of a standard 304 stainless steel plate (as illustrated in Fig. 1e) resulted in the balling and metalizing of the $Al_2O_3$. In this case, the heating had to be limited as the melting temperature of the steel plate is around 1400 °C and the S12 system was not capable of increasing the temperature above ~ 1100 °C due to the high heat loss. In the experiments, the plate was.

heated to 1050 °C which was too cold to support good melting conditions. Thereby, it was concluded that the standard build platform material must be exchanged for one that is more isolated from the PBF-EB chamber and has a higher temperature resistance. Such a material is proposed to be ceramic which is further tested in Sect. 3.2.2 and 3.2.3.

### 3.2.2 Heating and melting a loose $Al_2O_3$ powder bed

Using ceramic powder as a starting platform (as illustrated in Fig. 1g) was somewhat successful. Uncoated powder smoked instantly when the preheat from Sect. 3.1 was applied. The coated powder could be heated up to processing temperature (~ 1600 °C), and a flat powder bed was sustained although some powder particles were scattered away. The resulting powder cake consisted of some "untouched" and some melted particles that acted as a "solder" to bind the powder cake together as seen in Fig. 9a. The standard bridging that occurs for metals could not be observed but the cake was still solid enough to prevent smoke events. Melting on top of the powder bed with the process developed in Sect. 3.1 resulted in a lot of powder scattering. However, some experiments successfully melted ceramic powder and consolidated it to larger particles of a few millimeters as seen in Fig. 9b. On these particles, partially melted areas could be observed (Fig. 9c and e) where the powder has started to form isometric crystals. This correlates to the results earlier shown for the pre-sintered plates in Fig. 7d–f, where the material solidification takes place as a polycrystalline growth. An observation that could be made is that the heated powder changed color from grey (Ni coating) to white ($Al_2O_3$). In Fig. 9a, it can be noted visually that most of the particles

**Fig. 9** SEM micrographs of $Al_2O_3$ samples; sinter cake (**a**), melted particle of consolidated powder (**b**), close-up on isometric crystal formation on the melted particle (**c**)–(**d**) and nanoindentations on a prepared cross-section of a melted particle (**e**)
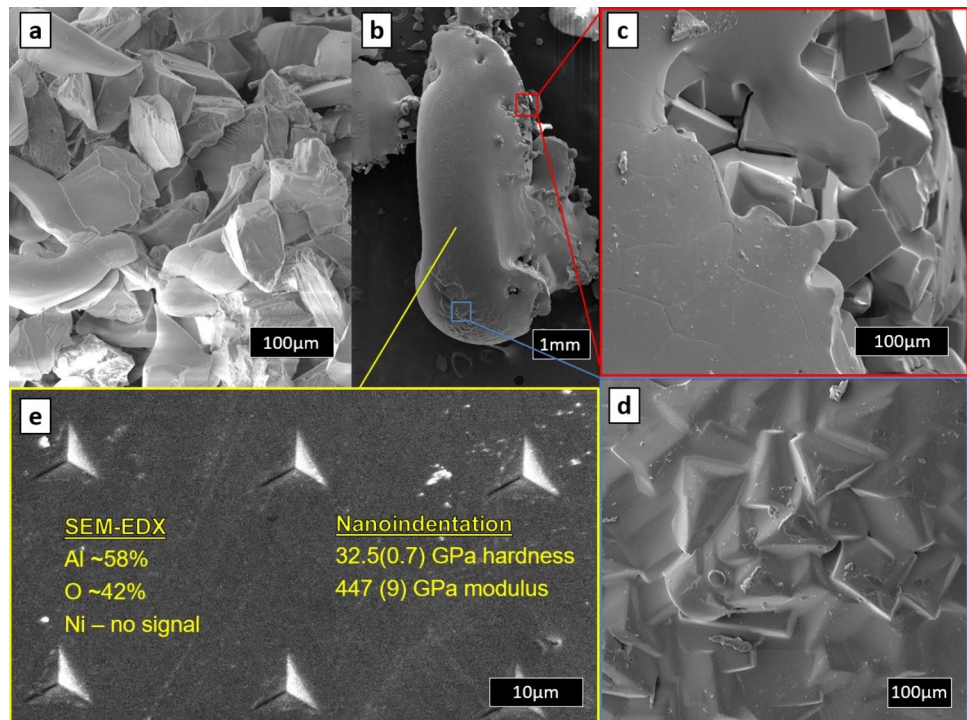


do not have any remnant Ni coating (compared to the initial state in Fig. 4b). In the lower part of Fig. 9a, a few particles with remaining coating can be seen. However, no Ni could be visually observed on any melted particles as is also true in Fig. 9b–d. Further analysis such as X-ray photoelectron spectroscopy (XPS) is needed to prove that the coating is removed. However as visually shown here, it is likely that most of the coating is removed during heating, and that the remnant coating is likely removed during melting. Some of the melted particles were nanoindented as shown in Fig. 9e. The measured average hardness from the 9 indentations performed in this section was 32.5 GPa with a standard deviation of 0.7 GPa. The high hardness and large melted particles further prove that PBF-EB energy is sufficient to melt ceramic materials.

### 3.2.3 Melting $Al_2O_3$ powder on top of a heated $Al_2O_3$ plate

Heating a pre-sintered $Al_2O_3$ plate presented no issues other than occasional cracks appearing early in the heating process. The cracks did not prevent further heating and were not considered a catastrophic problem as most cracks appear at low temperatures (probably resulting from pre-existing defects). Melting powder on top of the heated $Al_2O_3$ plate (as illustrated in Fig. 1f) was the most stable process condition that was tested in this study. In Fig. 10, a cross-section of four 70 μm layers of melted $Al_2O_3$ powder layers (right side) melted on top of a pre-sintered plate (left side) is shown. It can be noted how the left side of Fig. 10 has a lot of pores, as usually

indicative of a sintered ceramic, while the right side, produced from the consolidation of powder particles by EB-melting, is denser. Three rows of nanoindentations spaced by 25 μm are visible. The overlaid summary of these measurements shows a clear tendency that the melted material is ~ 7 GPa harder than the pre-sintered plate (after heating it in the process). In this section, the melted $Al_2O_3$ had a mean hardness of 35.3 GPa with a standard deviation of 1.6 GPa and a maximum measured hardness of 44.1 GPa. SEM–EDX of the sample showed no Ni signal and no Ni could be visually observed after the process. As previously mentioned, SEM–EDX cannot prove that there is no Ni present, but the lack of such a signal, and the fact that the process is taking place above the boiling point for Ni according to the calculations from Eq. (1) is indicative that most of the Ni has evaporated. These results prove that a layer-by-layer PBF-EB/C process is sustainable at least for four layers. After the melting of the four layers, thermal sintering of the Ni-coated $Al_2O_3$ powder inside the hopper caused degradation in the powder raking. Thereby, showing that although a rake-fed-hopper is good for initial process development, it cannot sustain a full AM process in this case.

## 4 Conclusions

The aim of this study was to investigate the feasibility of melting coated ceramic powder by the action of an electron beam to enable PBF-EB/C processes. A relatively large fraction of $Al_2O_3$ was selected for the study since the larger mass
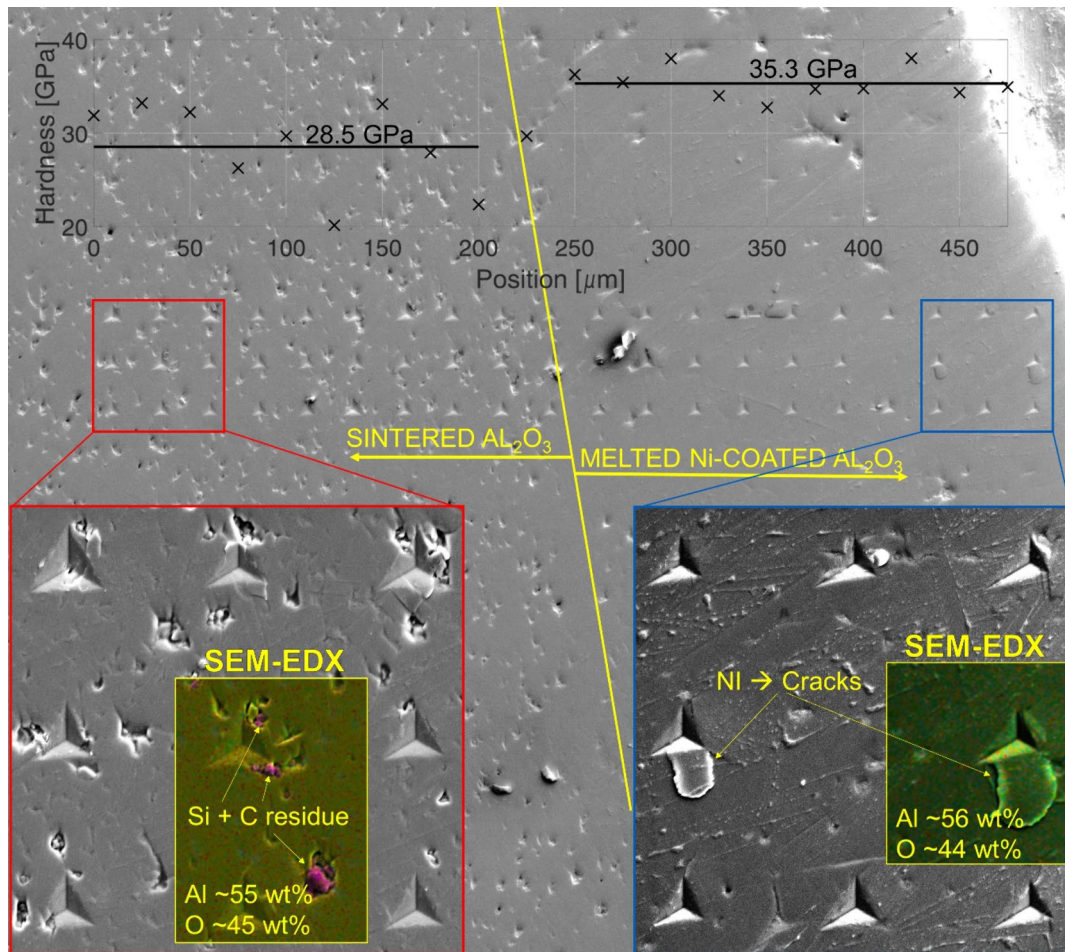
**Fig. 10** Cross-section of $Al_2O_3$ melted from 4 layers of powder (right) on top of a pre-sintered $Al_2O_3$ plate (left). Overlays show nanoindentation data* and closeups of different regions. *Nanoindentation hardness values below 70% of the mean were removed as well as values from indentations that were visually determined as bad to exclude errors arising from measurement as well as the collapse of the sintered structure

of the particles was hypothesized to decrease the smoke sensitivity. This powder was coated with ~ 1 μm of Ni, and the coating was shown to increase the powder bed conductivity by measuring the resistance over a standard volume of powder. The coating slightly increased the flowability but did not affect the powder packing properties.

Attempts to process uncoated $Al_2O_3$ powder by PBF-EB was also conducted, but as expected, it was not possible to process due to the high smoke sensitivity. The Ni-coated powder was successfully heated and melted, and results are promising regarding its processability in a layer-by-layer additive manufacturing process. Extended experiments are needed to investigate the processing of more than four consecutive layers as well as melting complex geometries. The presented work introduces a new method for functionalizing ceramic powders and a simple method for measuring the powder bed resistivity, which is crucial for understanding the smoke events. The work is also the first successful report

of a PBF-EB/C/$Al_2O_3$ process. Although the manufactured samples are not of complex geometries, the proposed coating approach is clearly shown as a promising route for enabling PBF-EB/C. The main conclusions can be summarized as follows:

- The tested Ni coating increased the electrical conductivity in the powder bed enough to avoid smoke. The coating also yielded slightly better flowability.
- Visual observation and SEM–EDX together with presented calculations suggest that no Ni is present in the melted regions after the process. Thereby, the Ni is assumed to be evaporated during the process.
- High temperatures are required for stable ceramic melting, sufficient penetration and crack-free material. The results show that the standard PBF-EB start plate and temperature monitoring equipment must be replaced to allow PBF-EB/C processes. In this study, a SWIR pyrom-

eter was used for measuring the temperature and ceramic start plates to enable stable melting conditions.

- Negative focus offsets (diverging beam) reduce melt spatter and probably charge build-up, but in this work the melt pool penetration was not sufficient to make use of such settings. The lower penetration at negative FO's is suggested to arise from the calibration method, which should be investigated in future work as other publications also have observed beneficial results in the negative FO-region.
- Low beam speeds resulted in unstable melt tracks, hole formation and increased cracking. In this work, 250–500 mm/s was found to be the absolute minimum feasible conditions and relatively stable conditions could be obtained at 1000–2000 mm/s.
- Spot melting was found to increase the tendency for cracks to appear during cold melting and thereby continuous melting was used for producing the samples. The standard bi-directional and uni-directional melting was also found to cause cracking and was replaced with a continuous converging melt line-scanning strategy.
- The hopper system used in this study places the powder too close to the heated build area, which causes unstable raking after only a few layers. For future work, the process can either be scaled up to use the standard hopper style or an alternative powder feeding system is needed.

**Data availability** The data that support the findings of this study are available from the corresponding author, W Sjöström, upon reasonable request.

## Declarations

**Conflict of interest** No potential conflict of interest was reported by the authors.

## References

1. Ullah A, Ur Rehman A, Salamci MU, Pıtır F, Liu T (2022) The influence of laser power and scanning speed on the microstructure and surface morphology of $Cu_2O$ parts in SLM. Rapid Prototyp J. 28(9):1796–1807. https://doi.org/10.1108/RPJ-12-2021-0342/FULL/PDF

2. Verga F, Makowska M, Cellerai G, Florio K, Schmid M, Wegener K (2021) Crack-healing, a novel approach for a laser-based powder bed fusion of high-performance ceramic oxides. Addit Manuf Lett 1:100021. https://doi.org/10.1016/J.ADDLET.2021.100021

3. Xing M et al (2022) SLM printing of cermet powders: Inhomogeneity from atomic scale to microstructure. Ceram Int 48(20):29892–29899. https://doi.org/10.1016/J.CERAMINT.2022.06.254

4. Zhou W, Kikuchi K, Nomura N, Yoshimi K, Kawasaki A (2020) In-situ formation of ceramic layer on Mo-based composites via laser powder bed fusion. Materialia 10:100655. https://doi.org/10.1016/J.MTLA.2020.100655

5. Sjöström W, Botero Vega CA (2023) Feasibility of electron beam melting metal coated ceramic powders. Accessed: Apr. 28, 2023. Available: https://urn.kb.se/resolve?urn=urn:nbn:se:miun:diva-46817

6. Sjöström W, Botero C, Jimenez-Pique E (2023) Coating as a methodology to increase processability of Al2O3 in electron beam powder bed fusion. Accessed: Apr. 28, 2023. Available: https://urn.kb.se/resolve?urn=urn:nbn:se:miun:diva-48006

7. Ladani L, Sadeghilaridjani M (2021) Review of powder bed fusion additive manufacturing for metals. Metals (Basel). https://doi.org/10.3390/met11091391

8. Sing SL, An J, Yeong WY, Wiria FE (2016) Laser and electron-beam powder-bed additive manufacturing of metallic implants: a review on processes, materials and designs. J Orthop Res 34(3):369–385. https://doi.org/10.1002/JOR.23075

9. Fu Z, Körner C (2022) Actual state-of-the-art of electron beam powder bed fusion. Eur J Mater 2(1):54–116. https://doi.org/10.1080/26889277.2022.2040342

10. Botero C et al (2020) Additive manufacturing of a cold-work tool steel using electron beam melting. Steel Res Int 91(5):1900448. https://doi.org/10.1002/SRIN.201900448

11. Zhang LC, Liu Y, Li S, Hao Y (2018) Additive manufacturing of titanium alloys by electron beam melting: a review. Adv Eng Mater 20(5):1700842. https://doi.org/10.1002/ADEM.201700842

12. Wu L et al (2021) Hot work tool steel processed by laser powder bed fusion: a review on most relevant influencing factors. Adv Eng Mater 23(7):2100049. https://doi.org/10.1002/ADEM.202100049

13. Azam FI, Abdul Rani AM, Altaf K, Rao TVVLN, Zaharin HA (2018) An In-depth review on direct additive manufacturing of metals. IOP Conf Ser Mater Sci Eng. https://doi.org/10.1088/1757-899X/328/1/012005

14. Laleh M et al (2022) Heat treatment for metal additive manufacturing. Prog Mater Sci. https://doi.org/10.1016/J.PMATSCI.2022.101051

15. Körner C (2016) Additive manufacturing of metallic components by selective electron beam melting—a review. Int Mater Rev 61(5):361–377. https://doi.org/10.1080/09506608.2016.1176289

16. Milberg J, Sigl M (2008) Electron beam sintering of metal powder. Prod Eng 2(2):117–122. https://doi.org/10.1007/s11740-008-0088-2

17. Chiba A, Daino Y, Aoyagi K, Yamanaka K (2021) Smoke suppression in electron beam melting of inconel 718 alloy powder based on insulator-metal transition of surface oxide film by mechanical stimulation. Material 14(16):4662. https://doi.org/10.3390/MA14164662

18. Galati M, Iuliano L (2018) A literature review of powder-based electron beam melting focusing on numerical simulations. Addit Manuf 19:1–20. https://doi.org/10.1016/J.ADDMA.2017.11.001

19. "JAM-5200EBM Electron Beam Metal AM Machine | Products | JEOL Ltd." https://www.jeol.co.jp/en/products/am/JAM-5200EBM.html (accessed May 12, 2022).

20. Cordero ZC, Meyer HM, Nandwana P, Dehoff RR (2017) Powder bed charging during electron-beam additive manufacturing. Acta Mater 124:437–445. https://doi.org/10.1016/J.ACTAMAT.2016.11.012

21. "NeuBeam - Wayland Additive Limited." https://www.waylandadditive.com/neubeam/ (accessed May 12, 2022).

22. "ProHeat – new innovation for powder heating without electron interaction | Freemelt." https://freemelt.com/mfn_news_en/proheat-new-innovation-for-powder-heating-without-electron-interaction/ (accessed May 12, 2022).

23. Sjöström W, Koptyug A, Rännar LE, Botero C (2024) Near-infrared radiation: a promising heating method for powder bed fusion. Mater Manuf Process 39(3):320–328 https://doi.org/10.1080/10426914.2023.2195910

24. Landau E et al (2020) Thermal characterization of the build chamber in electron beam melting. Addit Manuf 36(Auegst):101535. https://doi.org/10.1016/j.addma.2020.101535

25. Lin Z, Dabakhsh S, Rashid A (2022) Developing processing windows for powder pre-heating in electron beam melting. J Manuf Process 83(September):180–191. https://doi.org/10.1016/j.jmapro.2022.08.063

26. Arnold C, Böhm J, Körner C (2020) In operando monitoring by analysis of backscattered electrons during electron beam melting. Adv Eng Mater 22(9):1901102. https://doi.org/10.1002/ADEM.201901102

27. Ameen W, Al-Ahmari A, Ahmed N, Alshammary W, Salunkhe S, Hussein HMA (2021) Investigation the effect of electron beam melting parameters on overhang structure deformation. Mater Technol 37(10):1586–1593. https://doi.org/10.1080/10667857.2021.1994174

28. Lee HJ, Ahn DG (2021) Investigation of elimination of powder spreading in manufacture of thin and wide preheating beads from Co–Cr alloy powders using a P-ebeam. J Mater Res Technol 14:1873–1883. https://doi.org/10.1016/J.JMRT.2021.07.078

29. Murr LE et al (2012) Fabrication of metal and alloy components by additive manufacturing: examples of 3D materials science. J Mater Res Technol 1(1):42–54. https://doi.org/10.1016/S2238-7854(12)70009-1

30. Pasagada VKV, Yang N, Xu C (2022) Electron beam sintering (EBS) process for Ultra-High Temperature Ceramics (UHTCs) and the comparison with traditional UHTC sintering and metal Electron Beam Melting (EBM) processes. Ceram Int 48(7):10174–10186. https://doi.org/10.1016/J.CERAMINT.2021.12.229

31. Huo C, Tian X, Nan Y, Li D (2020) Hierarchically porous alumina ceramic catalyst carrier prepared by powder bed fusion. J Eur Ceram Soc 40(12):4253–4264. https://doi.org/10.1016/J.JEURCERAMSOC.2020.03.059

32. Hoon SR, Thomas AD, Linton PE (2009) The design and development of a closed chamber for the in-situ quantification of dryland soil carbon dioxide fluxes. Geogr Res 47(1):71–82. https://doi.org/10.1111/j.1745-5871.2008.00551.x

33. Lin Z, Zhao X, Dadbakhsh S, Rashid A (2021) Evaluating the electron beam spot size in electron beam melting machines. 14th Lamdamap conference (2021). http://urn.kb.se/resolve?urn=urn:nbn:se:kth:diva-292324

34. Prakash B, Gupta S, Malik P (2014) Characterization and testing of 30 kV, 60 kW electron optical column for melting applications. In: Proc. - Int. Symp. Discharges Electr. Insul. Vacuum, ISDEIV, pp 617–620. https://doi.org/10.1109/DEIV.2014.6961758

35. Suard M (2015) Characterization and optimization of lattice structures made by Electron Beam Melting. Doctorial thesis Université Grenoble Alpeshttps (2015). www.researchgate.net/publication/286677530_Characterization_and_optimization_of_lattice_structures_made_by_Electron_Beam_Melting

36. Helmer HE, Körner C, Singer RF (2014) Additive manufacturing of nickel-based superalloy Inconel 718 by selective electron beam melting: processing window and microstructure. J Mater Res 29(17):1987–1996. https://doi.org/10.1557/jmr.2014.192

37. Francis Z (2017) The effects of laser and electron beam spot size in additive manufacturing processes. Dissertations. Available: https://search.proquest.com/docview/1906683857?fromunauthdoc=true&pq-origsite=gscholar%0Ahttp://repository.cmu.edu/dissertations/909

38. Popov VV et al (2021) Powder bed fusion additive manufacturing using critical raw materials: a review. Materials (Basel) 14(4):1–37. https://doi.org/10.3390/ma14040909